ARTICLE   **Open Access**

Reversible colossal barocaloric effect dominated by disordering of organic chains in $(CH_3–(CH_2)_{n−1}–NH_3)_2MnCl_4$ single crystals

Yihong Gao[1,2], Hongxiong Liu[1,2], Fengxia Hu[1,2,3], Hongyan Song[1,2], Hao Zhang[1,2], Jiazheng Hao[1], Xingzheng Liu[1,2], Zibing Yu[1,2], Feiran Shen[1], Yangxin Wang[1,2], Houbo Zhou[1,2], Bingjie Wang[1,2], Zhengying Tian[1,2], Yuan Lin[1,2], Cheng Zhang[1,2], Zhuo Yin[1,2], Jing Wang[1,2,4], Yunzhong Chen[1], Yunliang Li[1,2,3], Youting Song[1], Youguo Shi[1,2,3], Tongyun Zhao[1,5], Jirong Sun[1,2,3], Qingzhen Huang[6] and Baogen Shen[1,2,3,7]

Abstract

Solid-state refrigeration based on the caloric effect is viewed as a promising efficient and clean refrigeration technology. Barocaloric materials were developed rapidly but have since encountered a general obstacle: the prominent caloric effect cannot be utilized reversibly under moderate pressure. Here, we report a mechanism of an emergent large, reversible barocaloric effect (BCE) under low pressure in the hybrid organic–inorganic layered perovskite $(CH_3–(CH_2)_{n−1}–NH_3)_2MnCl_4$ ($n = 9,10$), which show the reversible barocaloric entropy change as high as $\Delta S_r \sim 218, 230 \, J \, kg^{-1} \, K^{-1}$ at 0.08 GPa around the transition temperature ($T_s \sim 294, 311.5 \, K$). To reveal the mechanism, single-crystal $(CH_3–(CH_2)_{n−1}–NH_3)_2MnCl_4$ ($n = 10$) was successfully synthesized, and high-resolution single-crystal X-ray diffraction (SC-XRD) was carried out. Then, the underlying mechanism was determined by combining infrared (IR) spectroscopy and density function theory (DFT) calculations. The colossal reversible BCE and the very small hysteresis of 2.6 K (0.1 K/min) and 4.0 K (1 K/min) are closely related to the specific hybrid organic–inorganic structure and single-crystal nature. The drastic transformation of organic chains confined to the metallic frame from ordered rigidity to disordered flexibility is responsible for the large phase-transition entropy comparable to the melting entropy of organic chains. This study provides new insights into the design of novel barocaloric materials by utilizing the advantages of specific organic–inorganic hybrid characteristics.

Introduction

Refrigeration technology based on volatile hydro-fluorocarbon fluids gives rise to the destruction of the ozone layer and the greenhouse effect; thus, researchers have been exploring efficient and environmentally friendly alternative refrigeration materials. Ferroic materials, which exhibit a field-driven caloric effect near the ferroic transition, show the potential capacity to replace current refrigerants. Materials with an order-disorder transformation of magnetism can be driven by a magnetic field to induce magnetocaloric effects (MCEs). Analogously, the electrocaloric effects (ECE), elastocaloric effects (eCE) and barocaloric effects (BCE) can be induced in relevant materials by imposing an electric field, uniaxial stress and hydrostatic pressure, respectively[1]. Among these caloric effects, the barocaloric effect (BCE), as the last to be introduced, has evolved rapidly because it can be achieved universally in materials with volume-changed structural phase transitions. Well-known ferromagnetic and ferroelectric materials, such as $Gd_5Si_2Ge_2$, Mn_3GaN, $Fe_{49}Rh_{51}$,

BaTiO$_3$, and (NH$_4$)$_2$SO$_4$, also show considerable barocaloric effects in addition to MCEs or ECEs, where ferroic phase transitions are coupled with crystal deformation[1–8]. In addition, barocaloric effects have been reported in multiple materials where phase transitions are solely accompanied by structural change, which means dilation and/or shear[9–14]. Among the abundant barocaloric materials[9,11,12,14–20], some gratifyingly exhibit great barocaloric effects with isothermal entropy changes exceeding 100 J kg^{-1} K^{-1}, such as the fast ion conductor CaF$_2$[14], polyvinylidene di-fluoride-based polymers[18], Fe$_3$(bntrz)$_6$(tcnset)$_6$ with spin-crossover[20], and 1-Cl/Br-ada[19], originating from a melting-like freedom inflation of the sublattice, a reorientation of the polymeric chains with α-β phase transition, a switch between low and high spin states, and strong molecular orientational disorder, respectively. More attractively, the substantial BCE was discovered in various plastic crystals[12,13], which appear to be a milestone of BCE field. Plastic crystals NPG ((CH$_3$)$_2$C(CH$_2$OH)$_2$), PG ((CH$_3$)C(CH$_2$OH)$_3$), TRIS ((NH$_2$)C(CH$_2$OH)$_3$), and AMP ((NH$_2$)(CH$_3$)C(CH$_2$OH)$_2$) exhibit barocaloric entropy changes (ΔS_p) as high as 530 J kg^{-1} K^{-1} (0.57 GPa), 510 J kg^{-1} K^{-1} (0.25 GPa), 600 J kg^{-1} K^{-1} (0.25 GPa), and 690 J kg^{-1} K^{-1} (0.25 GPa), respectively[13,17], and the origin is closely related to the changes in the intermolecular hydrogen bonds and the orientational disorder across the phase transition[12,16].

The discovery of highly barocaloric materials has largely promoted solid-state barocaloric refrigeration techniques, and related theoretical models have been developed to simulate refrigeration processes[21,22]. However, only the reversible variables of the BCE (specifically, the reversible entropy change (ΔS_r) and adiabatic temperature change (ΔT_r)) can work for cooling during the pressurization and depressurization cycles. High latent heat is usually accompanied by a large hysteresis gap, which prevents the substantial BCE from being utilized at low pressures. For instance, plastic crystal NPG cannot produce useful BCE ($\Delta S_r = 0$) under 0.1 GPa in the refrigeration cycle owing to the ~14 K hysteresis[12], although its ΔS_p is as high as ~530 J kg^{-1} K^{-1} (0.57 GPa)[13]. Hence, exploring the reversible, substantial BCE driven by low pressure remains a high challenge.

Organic–inorganic perovskite hybrids are usually designed to generate targeted structures and properties by combining the desirable properties of inorganic materials (high electrical mobility, wide band gaps, thermal hardness) and organic compounds (highly efficient luminescence, high polarizability)[23]. For layered perovskite systems, larger and more complex organic cations can be accommodated to generate stable structures and hence functional properties, while organic cations in 3D perovskite systems are dimensionally required to fit into cubic perovskite structures, such as the methylammonium in MAPbI$_3$. By incorporating long-chain alkylammonium, organic–inorganic layered perovskites (CH$_3$–(CH$_2$)$_{n-1}$–NH$_3$)$_2$MnCl$_4$ were demonstrated to exhibit various functional properties, including thermal energy storage[24]. Very recently, Li et al. reported a reversible, substantial BCE in (CH$_3$–(CH$_2$)$_9$–NH$_3$)$_2$MnCl$_4$ ($n = 10$) polycrystalline powder[25], where the reversible barocaloric entropy change reaches $\Delta S_r \sim 250$ J kg^{-1} K^{-1} at a pressure of 0.1 GPa. Although powder X-ray diffraction (PXRD) and Raman scattering were performed, the exact structural information, particularly of the high-temperature phase, and the critical role of each component, including the NH$_3$ head, CH$_2$ and C–C chains, and CH$_3$ tails in the entire (CH$_3$–(CH$_2$)$_{n-1}$–NH$_3$)$^+$ chain, remain unclear due to the complex organic–inorganic hybrid structure and the polycrystalline nature of the samples[25]. In this article, we prepared (CH$_3$–(CH$_2$)$_{n-1}$–NH$_3$)$_2$MnCl$_4$ ($n = 9,10$) materials and successfully cultivated high-quality single crystals for $n = 10$. Then, the mechanism of the reversible, substantial BCE under low pressure was determined from high-resolution single-crystal X-ray diffraction (SC-XRD), infrared (IR) spectroscopy measurements, and density function theory (DFT) calculations. It was found that the (CH$_3$–(CH$_2$)$_{n-1}$–NH$_3$)$_2$MnCl$_4$ ($n = 10$) single crystals show latent heat entropy change as high as $\Delta S \sim 230$ J kg^{-1} K^{-1} across the phase transition ($T_s \sim 311.5$ K) upon heating, while thermal hysteresis as low as 2.6 K (0.1 K min^{-1}) and 4.0 K (1 K min^{-1}) was measured by differential scanning calorimetry (DSC). Accordingly, the barocaloric ΔS_p obtained by the quasi-direct method[17] reached a maximum under a low pressure of 0.04 GPa due to the extreme sensitivity of the phase transition to pressure, and the reversible entropy change (ΔS_r) after deducting irreversible part reaches the maximum under 0.08 GPa, i.e. $\Delta S_r \sim 230$ J kg^{-1} K^{-1}. (CH$_3$–(CH$_2$)$_{n-1}$–NH$_3$)$_2$MnCl$_4$ ($n = 9$) failed to grow a sufficient single crystal, and the corresponding thermal hysteresis was measured as 5.2 K (1 K min^{-1}), while $\Delta S_r \sim 212$ J kg^{-1} K^{-1} at 0.08 GPa. The reversible barocaloric performance of the both compositions are ahead of reported other barocaloric materials.

Materials and methods
Sample preparations

(CH$_3$–(CH$_2$)$_{n-1}$–NH$_3$)$_2$MnCl$_4$ ($n = 9,10$) single crystals are difficult to fabricate. To cultivate single crystals with high quality and suitable size, nucleation and crystal growth must occur slowly. Here, the preparation process was as follows. (CH$_3$–(CH$_2$)$_{n-1}$–NH$_3$)$_2$MnCl$_4$ ($n = 9,10$) was synthesized by a reaction in anhydrous ethyl alcohol. The *n*-nonylamine (C$_9$H$_{19}$NH$_2$) for $n = 9$ or *n*-decylamine (C$_{10}$H$_{21}$NH$_2$) for $n = 10$, hydrochloric acid (mass fraction of 0.37), and manganese dichloride tetrahydrate (MnCl$_2$·4H$_2$O) were weighed at a molar ratio of 2:2:1, and then added into the ethyl alcohol, the hydrochloric acid being added drop by drop. The mixture was heated and stirred under reflux for 6 h and then a precipitate appeared on slowly cooling.

During purification, the product was recrystallized at least three times with anhydrous ethyl alcohol. Then, after filtering and slow evaporation for one week without any motion and interference, a high-quality single crystal of $(CH_3-(CH_2)_{n-1}-NH_3)_2MnCl_4$ ($n=10$) was successfully obtained but no qualified single crystal was obtained for the $n=9$ material, despite much effort was dedicated. The reason for the difference in crystallization is probably the odd-even effect. Finally, the samples were placed in a vacuum desiccator at approximately 300 K to dry for 12 h and then preserved in a desiccator[26,27]. Although the resulting product for $n=9$ was similar in appearance to the $n=10$ single crystal, as both were pale pink fragments, we were unable to obtain regular diffraction information via SC-XRD (see Supplementary Information SI-1); the compared diffraction images of the $n=10$ single crystal and $n=9$ sample are shown in Fig. S1. From the diffraction image, the $n=9$ sample is not a good single crystal, although a partial stacking order was formed during the cultivation process, the structure of which was unable to be resolved via SC-XRD as done for the $n=10$ single crystal.

Characterization

High-resolution SC-XRD at variable temperatures was performed on a BRUKER D8 VENTURE with $\lambda=0.71073$ Å. The datasets of the $(CH_3-(CH_2)_{n-1}-NH_3)_2MnCl_4$ ($n=10$) were collected on heating at three temperatures, 298 K, 308 K, and 320 K, separately, below and above the transition temperature $T_s=311.5$ K. Only structural information at 298 K and 320 K will be discussed below, and other information is available in Supplementary Information SI-2. The data were corrected for absorption effects using the Multi-Scan method (SADABS). The structure was solved and refined using the Bruker SHELXTL Software Package. Relevant parameters about data collection and structure refinement are listed in Table S1, Table S2, and Table S3. Infrared (IR) spectroscopy was performed using a BRUKER TENSOR II Fourier transform infrared (FTIR) spectrometer in the frequency range of 900–4000 cm^{-1} with 1.5 cm^{-1} resolution. To characterize the barocaloric effect, heat flow under pressure was measured by a high-pressure differential scanning calorimeter (DSC) with a μDSC7 evo microcalorimeter (SETARAM, France). Specifically, the pressure of 0–0.1 GPa is applied by compressed N_2 gas with high purity (99.999%).
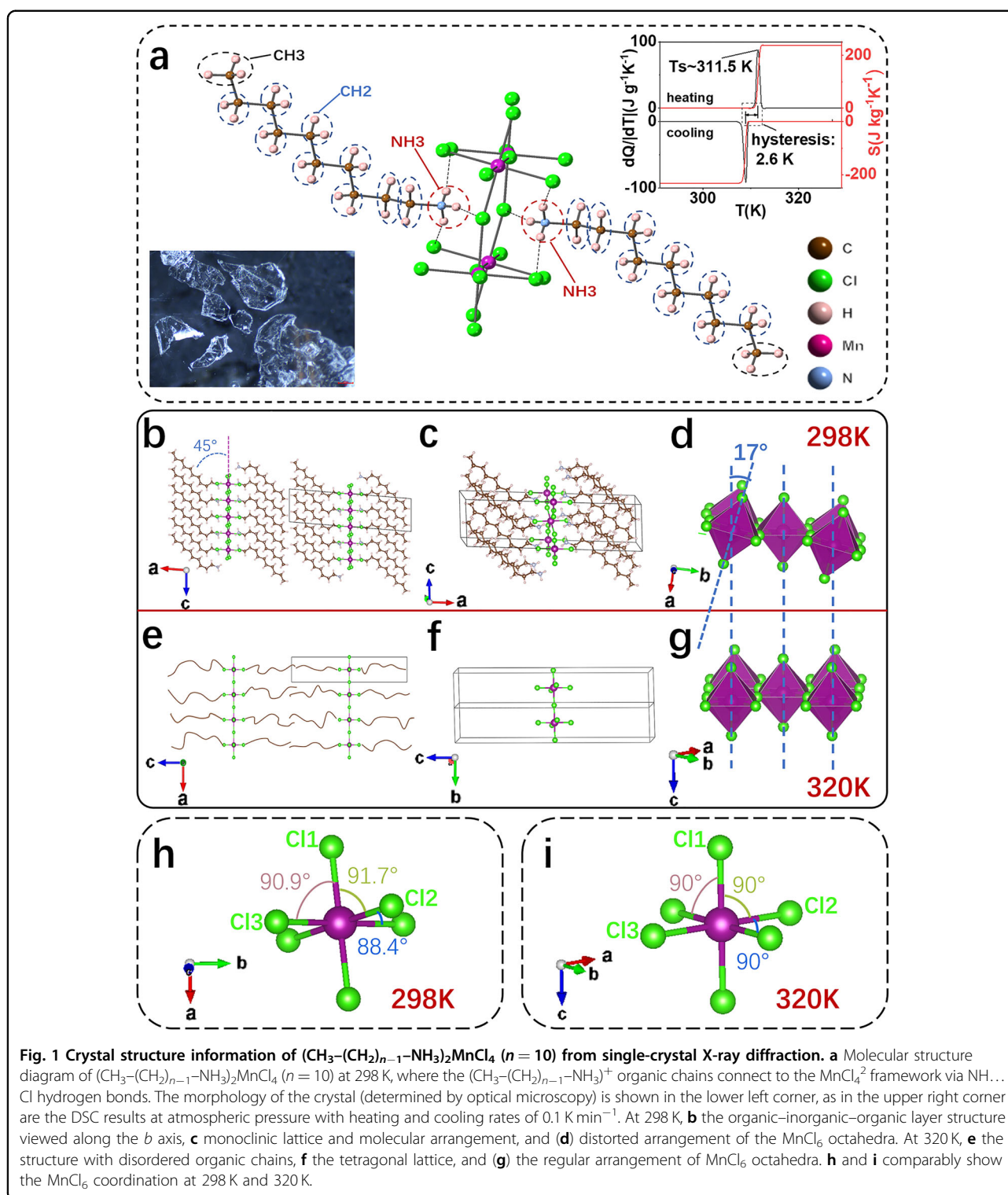
Density functional theory (DFT) calculations

The quantum mechanical calculations for the $(CH_3-(CH_2)_{n-1}-NH_3)_2MnCl_4$ ($n=10$) single crystal were performed using the Gaussian09 software package based on density functional theory (DFT). The B3LYP function with the 6-311 G* basis set was applied to optimize the molecular structure and to calculate the IR vibrational frequencies. The polarization function can better optimize the structure and frequency accuracy. The frequency correction factor is 0.97305. The energy convergence criterion is set at 10^{-6} eV throughout the calculations. The molecular optimization model at 298 K is based on atomic positions obtained from SC-XRD, where during the optimization process, the organic chain changes slightly under the energy convergence criterion but remains rigid.
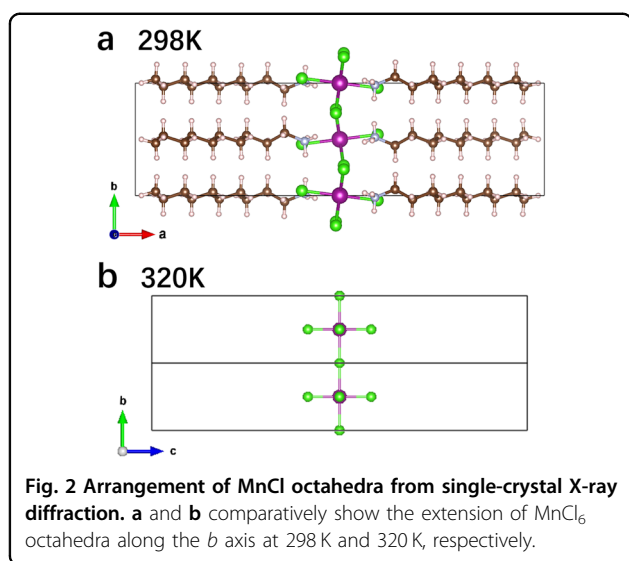
Results and discussion

The prepared $(CH_3-(CH_2)_{n-1}-NH_3)_2MnCl_4$ ($n=10$) single crystals appear as pale pink fragments, and the picture under the optical microscope is shown on the lower left of Fig. 1a. The heat flow at 1 bar (atmosphere pressure) with a heating and cooling rate of 0.1 K min^{-1} is shown on the upper right of Fig. 1a. A sharp first-order phase transition occurs near the transition temperature $T_s \sim 311.5$ K (peak position upon heating) with a large entropy change of approximately 230 J kg^{-1} K^{-1}. However, the thermal hysteresis is as small as 2.6 K defined as the distance between the maximums of the exothermal and endothermal peaks, and it is 1.5 K defined as the distance between the onsets of peaks, remarkably smaller than that of almost all other BCE materials, including plastic crystals. Hence, a large reversible BCE is expected.

To determine the mechanism of the high latent heat during the phase transition, high-resolution SC-XRD was performed at various temperatures to reveal the structural information on both sides of the phase transition, and the results are given in Fig. 1b–i (the parameters for data collection and structural refinement are shown in Tables S1–3). The careful refinements revealed that in the low-temperature phase at 298 K, $(CH_3-(CH_2)_9-NH_3)_2MnCl_4$ has a monoclinic layered perovskite structure with space group $P2_1/c$ and lattice parameters $a=26.7$ Å, $b=7.3$ Å, $c=7.2$ Å, $\alpha=\gamma=90°$, $\beta=94.6°$; the unit cell is framed in black in Fig. 1b, c. Each unit cell contains two $MnCl_6$ octahedrons and four organic chains. The layers are connected via van der Waals interactions through the methyl group at each tail of an organic chain, as shown in Fig. 1b for two adjacent layers. Each layer has a sandwich-like organic–inorganic–organic structure with a $MnCl_4^{2-}$ inorganic framework connecting tightly to the $(CH_3-(CH_2)_9-NH_3)^+$ organic chains on both sides. In the $MnCl_4^{2-}$ inorganic framework, the octahedron $MnCl_6$ coordinate is two-dimensionally extended by ionic-covalent interactions in the bc plane, while the $(CH_3-(CH_2)_9-NH_3)^+$ organic chains on both sides remain in parallel at an angle of 45° with the Mn atom column when viewed along the b axis (Fig. 1b). The inorganic framework is connected to the organic moieties through the NH_3 heads, which interact with the chlorine atoms of the $MnCl_4^{2-}$ framework via hydrogen bonds (N–H...Cl), and each $(CH_3-(CH_2)_9-NH_3)^+$ chain contains one NH_3 head,

Fig. 1 Crystal structure information of (CH₃–(CH₂)ₙ₋₁–NH₃)₂MnCl₄ (n = 10) from single-crystal X-ray diffraction. a Molecular structure diagram of $(CH_3-(CH_2)_{n-1}-NH_3)_2MnCl_4$ (n = 10) at 298 K, where the $(CH_3-(CH_2)_{n-1}-NH_3)^+$ organic chains connect to the $MnCl_4^2$ framework via NH… Cl hydrogen bonds. The morphology of the crystal (determined by optical microscopy) is shown in the lower left corner, as in the upper right corner are the DSC results at atmospheric pressure with heating and cooling rates of 0.1 K min⁻¹. At 298 K, **b** the organic–inorganic–organic layer structure viewed along the *b* axis, **c** monoclinic lattice and molecular arrangement, and (**d**) distorted arrangement of the $MnCl_6$ octahedra. At 320 K, **e** the structure with disordered organic chains, **f** the tetragonal lattice, and (**g**) the regular arrangement of $MnCl_6$ octahedra. **h** and **i** comparably show the $MnCl_6$ coordination at 298 K and 320 K.

nine methylene (CH₂), and one methyl (CH₃) tail in sequence (Fig. 1a). Due to the tight bonding of organic moieties with the inorganic frame, the alignments of the inorganic $MnCl_6$ octahedra twist in the low-temperature phase (see Fig. 1d); the details of the distortion angles refined from SC-XRD are shown in Table S4. The adjacent octahedrons at 298 K show an apparent stagger angle of 17°, which differs from that of the high-temperature phase at 320 K (Fig. 1g). The distinct difference between the staggered and regular extensions of the $MnCl_6$

Fig. 2 Arrangement of MnCl octahedra from single-crystal X-ray diffraction. a and **b** comparatively show the extension of MnCl$_6$ octahedra along the *b* axis at 298 K and 320 K, respectively.

octahedra along the *b* axis at 298 K and 320 K is shown in Fig. 2a, b. Moreover, the octahedral coordination of MnCl$_6$ at 298 K is noticeably deformed, with angles of 91.7° for Cl1−Mn−Cl2, 90.9° for Cl1−Mn−Cl3, and 88.4° for Cl2−Mn−Cl3 (Fig. 1h), while all those in the high-temperature phase at 320 K are 90° (Fig. 1i). More detailed structural diagrams of (CH$_3$−(CH$_2$)$_9$−NH$_3$)$_2$MnCl$_4$ are shown in Fig. S5−13.

At 320 K (the high-temperature phase above T_s), (CH$_3$−(CH$_2$)$_9$−NH$_3$)$_2$MnCl$_4$ transforms to a tetragonal structure with space group P4/mmm and parameters $a = b = 5.2$ Å, $c = 28.3$ Å, and $\alpha = \beta = \gamma = 90°$; the unit cell is framed in black (Fig. 1e, f). One unit cell contains one MnCl$_6$ octahedron and two (CH$_3$−(CH$_2$)$_9$−NH$_3$)$^+$ chains due to the change in symmetry of the space group. More differently, only a fourfold symmetric MnCl$_4^{2-}$ inorganic framework can be detected, while the organic chains become unobservable under X-ray excitation. The lack of diffraction information from the organic moieties indicates the broken spatial translation symmetry, strongly implying that the organic moieties have become highly disordered in the high-temperature phase; the irregular organic chains are schematically drawn in brown and shown in Fig. 1e. The MnCl$_6$ coordination octahedra at 320 K become completely parallel and exhibit translation invariance, while the angles of the Cl1−Mn−Cl2, Cl1−Mn−Cl3, and Cl2−Mn−Cl3 bonds are all 90°. The decrease in torsion of the MnCl$_6$ octahedron arrangement strongly suggests remarkable weakening or even breaking of the hydrogen bonds between the organic cations and inorganic anions, further supporting the disordering of organic chains at the high-temperature phase.

To obtain details about the change in the organic (CH$_3$−(CH$_2$)$_9$−NH$_3$)$^+$ chains (Fig. 3a) from ordering to

disordering and understand the large entropy change across the phase transition T_s, we performed IR spectroscopy in the frequency range of 900−4000 cm^{-1} with a 1.5 cm^{-1} resolution at variable temperatures from 288 K to 338 K upon heating. As shown in Fig. 3b−g, specific vibration bands were selected to illustrate the change in intrachain motion before and after transition; these vibration bands provide information on all the NH$_3$, CH$_2$, CH$_3$ groups and C−C chains from head to tail throughout the organic moieties. The assignments of the bands are listed in Table S7, and the complete infrared spectra are shown in Fig. S14.

As shown in Fig. 3b, the vibration bands near 1490 cm^{-1} (trajectory displayed with black line) and 1580 cm^{-1} (trajectory displayed with purple line) are assigned to the symmetric and asymmetric bending vibrations of the NH$_3$ head, respectively. The sharp red-shift across T_s upon heating (Fig. 3b, c) indicates that the NH$_3$ bending frequency suddenly decreases as the order state collapses, which illustrates the weakening of hydrogen bonds of NH$_3$[28], i.e. the N−H…Cl connections between the organic chains and the inorganic framework, at the disorder state above T_s, in line with the torsion disappearance of MnCl$_6$ octahedron revealed by SC-XRD. On the left side close to the NH$_3$ symmetric bending band, two bands at 1462 cm^{-1} and 1474 cm^{-1} corresponding to the CH$_2$ scissoring vibration (the body of organic moieties, Fig. 3a) can be identified at the ordered state below T_s. These bands suddenly merge into a single band as the ordered state collapses at T_s (Fig. 3b, c). The presence of the two bands (correlation splitting) of the CH$_2$ scissoring modes at the order phase is caused by C−C chain and interchain interactions in between. The CH$_2$ vibration modes often split into two components due to interchain interactions in closely packed alkyl chain systems where more than one chain is present per unit cell[29]. The collapse of the two bands into a single band suggests the weakening or even disappearance of the CH$_2$ interchain interactions at the disorder phase above T_s. Furthermore, as shown in Fig. 3d, e, similar to CH$_2$ bending, the splitting of CH$_2$ wagging vibration below T_S also merges into a single band as soon as the ordered state collapses, further illustrating the sudden weakening or disappearance of the CH$_2$ interchain interactions at the disorder high-temperature phase.

For the CH$_3$ tails of the organic chains, the peaks at 2869 and 2953 cm^{-1} represent the symmetric and asymmetric C−H stretching vibration of CH$_3$, respectively (Fig. 3g, black lines), while the peak at 1375 cm^{-1} corresponds to its symmetric deforming mode[30] (Fig. 3d). All three undergo a sudden blueshift as soon as the ordered state collapses at T_s. The increase in frequency of the CH$_3$ stretching and deforming vibrations implies that the CH$_3$ tails of organic chains become less restricted and freer, which strongly

Fig. 3 Infrared spectra of $(CH_3–(CH_2)_9–NH_3)_2MnCl_4$ at variable temperatures from 288 K to 338 K collected while heating. a Structure of the unilateral organic chain and the conterminous part of the inorganic framework part. **b** Infrared spectra in the region of 1400–2000 cm^{-1} involving CH_2 scissoring and NH_3 bending vibrations and the C–NH_3^+ band, and (**c**) the corresponding band frequencies vs. temperature. **d** Infrared spectra in the region of 1000–1400 cm^{-1} containing the CH_2 wagging and CH_3 symmetric deforming vibrations, and (**e**) the corresponding CH_2 wagging band frequencies vs. temperature. **f** Infrared spectra in the region of 2000–3300 cm^{-1}, showing the bands of the C–H stretching vibration (2800–3000 cm^{-1}) and NH_3 stretching vibrations (purple zone). **g** Infrared spectra concerning C–H stretching vibrations of CH_2 and CH_3 with a magnified view of the corresponding area shown in (**f**).

suggests the weakened interlayer van der Waals interactions between the two adjacent layers (Fig. 1b) in the disordered state of the high-temperature phase. Moreover, the symmetric and asymmetric C–H stretching vibrations of the CH_2 group arising at 2853 and 2923 cm^{-1} (Fig. 3g, red lines), respectively[31], are both more intense than those of the CH_3 group, which is understandable considering the higher ratio of $CH_2/CH_3 = 9/1$ in a single $(CH_3–(CH_2)_9–NH_3)^+$ chain.

Moreover, the IR spectra reveal information regarding the C–C...–C–N skeleton of the organic chains, which become flexible across the order-disorder phase transition. In Fig. 3d, except for the CH_2 wagging vibration and CH_3 symmetric deforming bands, other multiple bands from 1000 to 1300 cm^{-1} mainly stem from the skeletal vibrations that occur in the carbon chain, specifically the C–C stretching and bending vibrations. With the occurrence of a phase transition from an ordered to disordered state, the bands broaden and weaken, indicating the rigidity–flexibility transition of C–C chains. This result indicates that the carbon bonds weaken, and various conformers may appear, leading to wider bands in the disordered phase. Moreover, the broad band near 1880 cm^{-1} corresponds to the presence of C–NH_3^{+}[30], (Fig. 3b) and its sudden redshift at T_s indicates the weakened bonding energy of C–N as the organic chains undergo a rigidity–flexibility change across the T_s. Figure 3f shows the bands of C–H and N–H stretching vibrations. In the 3000–3200 cm^{-1} region of the N–H stretching vibration of the NH_3 group (the purple zone), the bands broaden across the order-disorder phase transition. It can be surmised that the various conformations of the C–C chain cause the various stretching vibrations of the NH_3 head; thus, more vibration modes may appear, and their superposition leads to broader bands in the disordered state. In the range of 2300–2800 cm^{-1} (the pink area in Fig. 3f), multiple unidentified bands broaden and weaken above T_s, which also reflects the rigidity–flexibility transition of the organic chains analogous to the C–C skeleton vibration within the 1000–1300 cm^{-1} range.

Li et al. investigated the disordering process in (CH_3–$(CH_2)_{n-1}$–$NH_3)_2MnCl_4$ ($n = 10$) by Raman scattering[25], which mainly analyzes the conformational disordering of C-C organic chains. The 1065, 1109, 1146, and 1174 cm^{-1} bands in the range of 1000–1200 cm^{-1} were assigned to the trans-conformation of C–C skeleton vibrations in the Raman spectra, which all disappeared in the high-temperature phase, suggesting that the conformation of long trans planar chains changed across the T_s[25]. Evidence of gauche bond appearance was speculated in the decrease of 1465 cm^{-1} shoulder, which corresponds to intramolecular coupling of trans structures. Additionally, Raman spectra collected in the low-frequency region provided more information on conformational disordering of C–C chains[25]. The 235 cm^{-1} band corresponding to the accordion-like longitudinal acoustic mode (LAM) disappeared, and only a broad, weak band was observed near 247 cm^{-1} at high-temperature phase, which also means that the conformation of the long trans planar chains changed[25]. The conformation change from trans planar chains to gauche bond structure reflects the deforming/twisting of organic C–C chains during the disordering process. Our IR spectrometer works in

middle wavenumber region. Analogous to the Raman spectra, the corresponding trans bands possibly arise at approximately 1060, 1106, 1143, and 1176 cm^{-1} (Fig. 3d). The peak at 1060 cm^{-1} disappears and the peak at 1106 cm^{-1} becomes weak in the high-temperature phase, in line with the Raman results, while the last two overlap with the CH_2 wagging bands.

In summary, the drastic transformation from ordered rigidity to disordered flexibility in the organic chains rationalizes the aforementioned absence of diffraction information for the organic moieties by SC-XRD and rationalizes the substantial phase-transition entropy comparable to the melting entropy of organic chains.

To clarify the conformation of the organic moiety at the high-temperature state, DFT (density function theory) calculations were performed to speculate the possible conformational change with the phase transition. The atomic positions of the (CH_3–$(CH_2)_9$–$NH_3)^{+}$ organic chain at 298 K obtained from SC-XRD were added, and the calculated model is shown in Fig. 4a. Then impose the dihedral of adjacent C–C bonds varying on the structural model at 298 K, and the computational results suggest an optimization model of molecule for high-temperature state at 320 K as seen in Fig. 3b, exhibiting flexible conformation. The DFT calculations show that at the high-temperature state, the carbon chains get twisted possessing changed C–C bond angles and lengths in comparison with the rigid trans-conformation at the low-temperature phase. The simulated IR spectra of the two models for
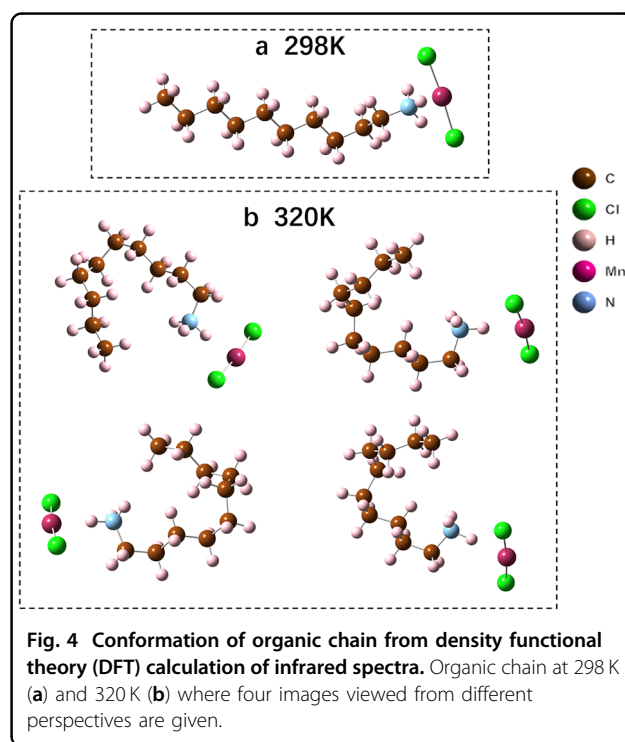

Fig. 4 Conformation of organic chain from density functional theory (DFT) calculation of infrared spectra. Organic chain at 298 K (**a**) and 320 K (**b**) where four images viewed from different perspectives are given.

Table 1 For specific vibrational modes, the comparison of experimental IR results and theoretical results calculated by DFT.

Vibration mode	Wavenumber (cm^{-1})			
	298 K exp.	320 K exp.	298 K calc.	320 K calc.
CH$_2$ scissoring	1462, 1473	1467	1488, 1496	1496
NH$_3$ asymmetric bending	1584	1577	1577	1562
C–NH$_3^+$	1881	1837	1875	1871
CH$_3$ symmetric deforming	1373	1378	1378	1389
CH$_3$ asymmetric stretching	2953	2957	2932	2944

specific vibration modes are comparatively given with the experimental results in Table 1. The calculated behaviors across the phase transition are roughly consistent with those obtained from experimental measurements, which verifies the rationality of the possible conformation of organic chains at 320 K, as shown in Fig. 4b.

Concretely, for the NH$_3$ group at the head of organic chain, the DFT calculation indicates that the vibration modes of NH$_3$ asymmetric bending and C–NH$_3^+$ bands both get redshifted across the order-disorder phase transition in analogy to the experimental results (Fig. 3b). Therefore, the vibrational variation of the NH$_3$ group is verified to be relevant to weakened N–H...Cl hydrogen bonds and softened C–C...–C–N chain skeleton. For the body of the organic chain, the calculated double bands of CH$_2$ scissoring vibration at low-temperature phase collapse to a single one at high-temperature phase, consistent with the experimental measurements (Fig. 3b), and for the CH$_3$ group at the tail of the organic chain, the calculated symmetric deforming and asymmetric stretching vibrations both get blueshift on heating across T_s, also consistent with experimental measurements (Fig. 3d, g). The calculations demonstrated that, as for the vibration modes of CH$_2$ and CH$_3$ groups, their change with phase transition is closely relevant to the bended and softened chain conformation at high-temperature phase, which actually point to the weakening of the interchain interaction and the interlayer van der Waals interaction above T_s.

In summary, by utilizing DFT computation, a reasonable conformation of the organic chain in the high-temperature phase is visualized with a twisted and softened C–C chain skeleton. The calculated results vividly illustrate the changes in the organic chain across the T_s, which is also an aspirational need of Raman research about the change of conformational ordering of C–C chains[25].

An early study[32] also investigated the dynamic process involving the order-disorder transition by combining an incoherent neutron scattering (INS) experiment with theoretical simulations for (CH$_3$–(CH$_2$)$_9$–NH$_3$)$^+$ decylammonium chains in a polycrystalline sample (CH$_3$–(CH$_2$)$_9$–NH$_3$)$_2$MnCl$_4$. It was concluded that, in the high-temperature phase, the chains can adopt a stabilized 'kink' conformer (t$_4$gtg't, where t indicates a trans bond and g indicates a gauche bond in organic chains) and move fastly related to both conformational interconversions and cooperative torsions along the main chain axis. When the temperature continuously rises above the transition, the degree of conformational disorder and cooperative torsion drastically increase. That is, different temperatures may correspond to different levels of conformational disorder. The 'kink' conformer (t$_4$gtg't) shows some differences from our results calculated by DFT. In addition to the temperature, the different experimental methodologies and theoretical models may also cause some differences due to the complexity of organic-based molecules.

The intrinsic thermally induced entropy change of barocaloric materials that occurs under atmospheric pressure usually plays a dominant role in determining the upper limit of entropy change induced by finite pressure. In some cases, the contributions beyond the transition cannot be ignored[13]. The large entropy change of approximately 230 J kg^{-1} K^{-1} demonstrates the great potential for a large BCE in (CH$_3$–(CH$_2$)$_{n-1}$–NH$_3$)$_2$MnCl$_4$ ($n=10$). A phase transition with large latent heat generally exhibits large hysteresis due to the high energy barrier of the phase transition. Unusually, the (CH$_3$–(CH$_2$)$_{n-1}$–NH$_3$)$_2$MnCl$_4$ ($n=10$) single crystal was measured to have very small hysteresis of 2.6 K at a temperature ramping rate of 0.1 K min^{-1} (upper inset of Fig. 1a) and 4.0 K at 1 K min^{-1} (Fig. 5a), originating from the single-crystal nature lacking effect from the grain boundary, as well as the specific hybrid organic–inorganic structure, which greatly facilitates achieving large reversible BCE. For (CH$_3$–(CH$_2$)$_{n-1}$–NH$_3$)$_2$MnCl$_4$ ($n=9$), which failed to grow a high-quality single crystals, the measured entropy change across $T_s \sim 294$ K by DSC was approximately 212 J kg^{-1} K^{-1}, while the thermal hysteresis was 5.2 K at a ramping rate of 1 K min^{-1} (Figs. S15–17).

To verify the large BCE and its reversibility in (CH$_3$–(CH$_2$)$_{n-1}$–NH$_3$)$_2$MnCl$_4$ ($n=9$, 10), we performed heat flow measurements by high-pressure DSC and used a quasi-direct method to evaluate the BCE[1,33], as shown in Fig. 5 and Figs. S16–22. From the heat flow curves shown in Fig. 5a and Fig. S16, we determined the temperature-dependent entropy with the specific heat capacity (C_p) considered and not, as shown in Fig. 5b and Fig. S23 for the (CH$_3$–(CH$_2$)$_{n-1}$–NH$_3$)$_2$MnCl$_4$ ($n=10$) single crystal and Figs. S18 and Fig. S17 for the (CH$_3$–(CH$_2$)$_{n-1}$–NH$_3$)$_2$MnCl$_4$ ($n=9$) sample. The measured C_p is
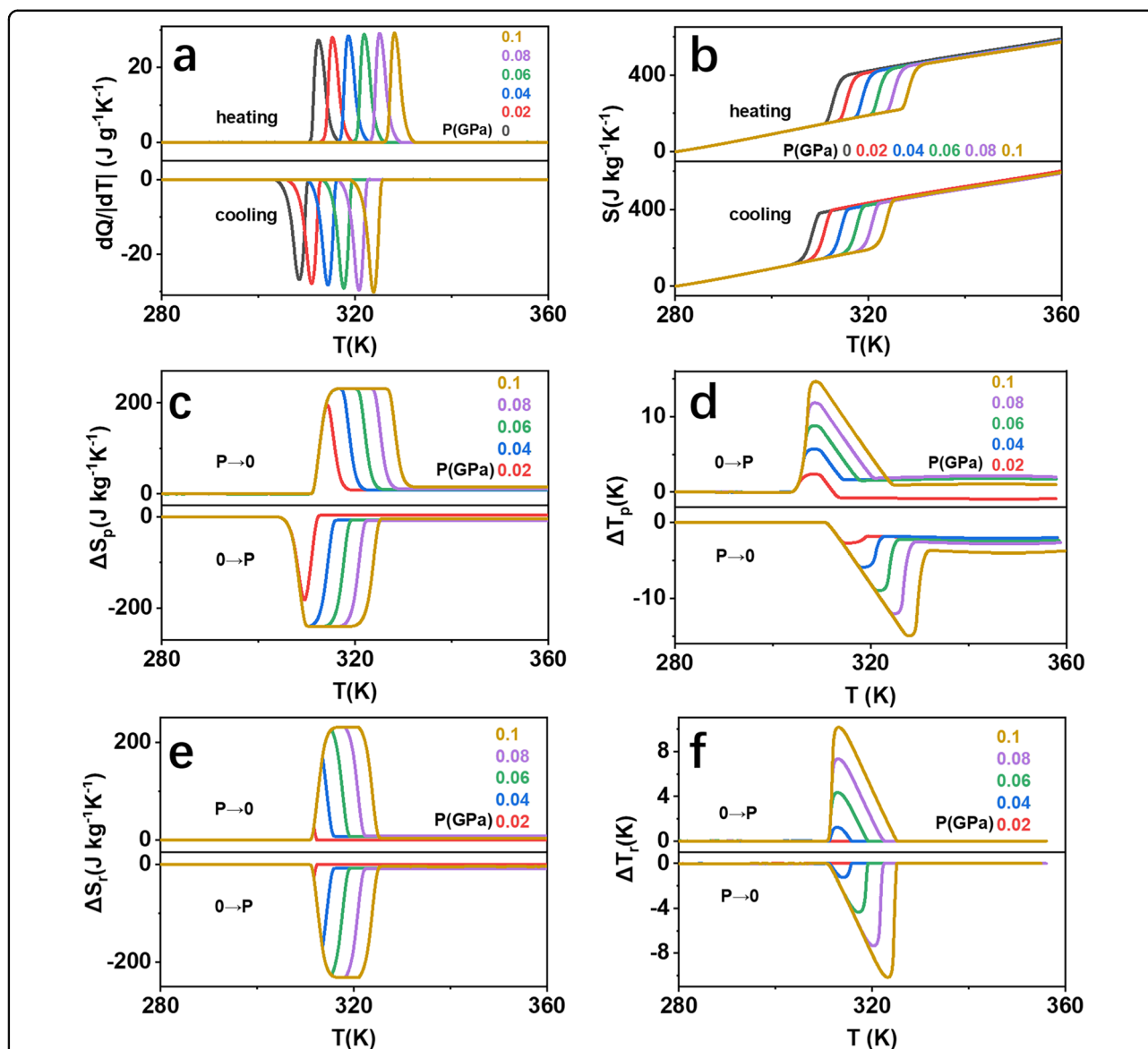
Fig. 5 Barocaloric performance of (CH$_3$-(CH$_2$)$_9$-NH$_3$)$_2$ MnCl$_4$ single crystal. a Heat flow measured at a rate of temperature of 1 K min^{-1} under selected pressures and (**b**) the resultant entropy–temperature curves that take into account the specific heat. **c** Isothermal entropy change ΔS_p induced by pressurization (downside) and depressurization (upside), given by the isothermal subtraction of the entropy curves in (**b**). **d** Adiabatic temperature change ΔT_p induced by pressurization (downside) and depressurization (upside), given by isentropic subtraction of entropy curves in (**b**). The atmospheric pressure/P is considered the initial value for the compression/decompression process during subtraction. **e** Reversible isothermal entropy change ΔS_r obtained by overlapping pressurization-induced and depressurization-induced isothermal entropy change curves in (**c**). **f** Reversible adiabatic temperature change ΔT_r obtained excluding the influence of thermal hysteresis[10,19].

provided in Fig. S24 and Fig. S25 for the $n = 10$ and $n = 9$ materials, respectively. One can find that the T_s was extremely pressure-sensitive and had a driving speed as high as ~150 and ~172 K GPa^{-1} when $n = 10$ and $n = 9$, respectively (Table 2). By subtracting the variable-pressure entropy–temperature curves at constant temperature or entropy, we obtain the pressure-induced entropy change ΔS_p (Fig. 5c, Fig. S19) and adiabatic

temperature change ΔT_p (Fig. 5d, Fig. S20), where the atmospheric pressure is taken as the initial value for compression and the pressure P is taken as the initial value for the decompression process. A low pressure of 0.04 GPa is sufficient to completely drive the phase transition for the $n = 10$ single crystal, producing the maximum isothermal $\Delta S_p \sim 230$ J kg^{-1} K^{-1} (Fig. 5c). For the $n = 9$ sample, 0.06 GPa produces the maximum

Table 2 Barocaloric materials with phase-transition entropy changes larger than 100 J kg^{-1} K^{-1}.

Compounds	Δp (G Pa)	T_s (cooling) (K)	$\lvert \Delta S_p \rvert$ (J kg^{-1} K^{-1})	Hys.(K) T rate (K/min)	dT_s/dP (K/GPa)	$\lvert \Delta S_r \rvert$ (J kg^{-1} K^{-1})	$\lvert \Delta T_r \rvert$ (K)	Ref.
NPG (CH$_3$)$_2$C(CH$_2$OH)$_2$	0.091	300	384	14 (0.1)	75	0	0	[12]
NPG (CH$_3$)$_2$C(CH$_2$OH)$_2$	0.57	300	530 ± 5	19 ± 1 (2)	93 ± 18	510	30	[13,17]
NPG (CH$_3$)$_2$C(CH$_2$OH)$_2$	0.1	300	405 ± 5	19 ± 1 (2)	93 ± 18	0	0	[13,17]
TRIS (NH$_2$)C(CH$_2$OH)$_3$	0.25	331.2 ± 0.5	600 ± 60	75 (2–4)	15 ± 6	0	0	[17]
TRIS (NH$_2$)C(CH$_2$OH)$_3$	0.1	331.2 ± 0.5	445 ± 5	75 (2–4)	15 ± 6	0	0	[17]
PG (CH$_3$)C(CH$_2$OH)$_3$	0.25	350.5 ± 0.5	510 ± 50	4 (2–4)	94 ± 3	500 ± 5	10 ± 1	[17]
PG (CH$_3$)C(CH$_2$OH)$_3$	0.1	350.5 ± 0.5	445 ± 5	4 (2–4)	94 ± 3	155 ± 5	1	[17]
AMP (NH$_2$)(CH$_3$)C(CH$_2$OH)$_2$	0.25	–	690 ± 70	–	85 ± 7	0	0	[17]
AMP (NH$_2$)(CH$_3$)C(CH$_2$OH)$_2$	0.1	–	600 ± 5	–	85 ± 7	0	0	[17]
NPA (CH$_3$)$_3$C(CH$_2$OH)	0.27	211.3 ± 0.5	330 ± 30	20 (2–4)	119 ± 2	250 ± 5	16 ± 1	[17]
NPA (CH$_3$)$_3$C(CH$_2$OH)	0.1	211.3 ± 0.5	245 ± 5	20 (2–4)	119 ± 2	0	0	[17]
CaF$_2$	–	1400*	225.6	–	–	–	–	[14]
1-Cl-ada	0.1	245	170 ± 5	9 (2–4)	270	160 ± 5	16 ± 1	[19]
1-Br-ada	0.1	308	150 ± 5	9 (2.5–3)	333	135 ± 5	21 ± 1	[19]
Fe$_3$(bntrz)$_6$(tcnset)$_6$	0.055	316	–	2 (2)	250	80	10	[20]
Fe$_3$(bntrz)$_6$(tcnset)$_6$	0.26	316	–	2 (2)	–	120	35	[20]
(CH$_3$–(CH$_2$)$_9$–NH$_3$)$_2$MnCl$_4$	0.1	306 ± 1	250	9 (2)	–	~250	~12	[25]
(CH$_3$–(CH$_2$)$_8$–NH$_3$)$_2$MnCl$_4$	0.1	289.1 (294.3*)	212	5.2 (1)	172	212	10	This work
(CH$_3$–(CH$_2$)$_9$–NH$_3$)$_2$MnCl$_4$ single crystal	–	308.9 (311.5*)	–	2.6 (0.1)	–	–	–	This work
	0.1	308.4 (312.4*)	230	4.0 (1)	150	230	10	

The phase-transition temperature (T_s), hysteresis (Hys.) at atmospheric pressure measured by DSC where the temperature ramping rate is also given, the pressure sensitivity (dT_s/dP), barocaloric entropy change (ΔS_p), reversible barocaloric entropy change (ΔS_r) and adiabatic temperature change (ΔT_r) are listed.
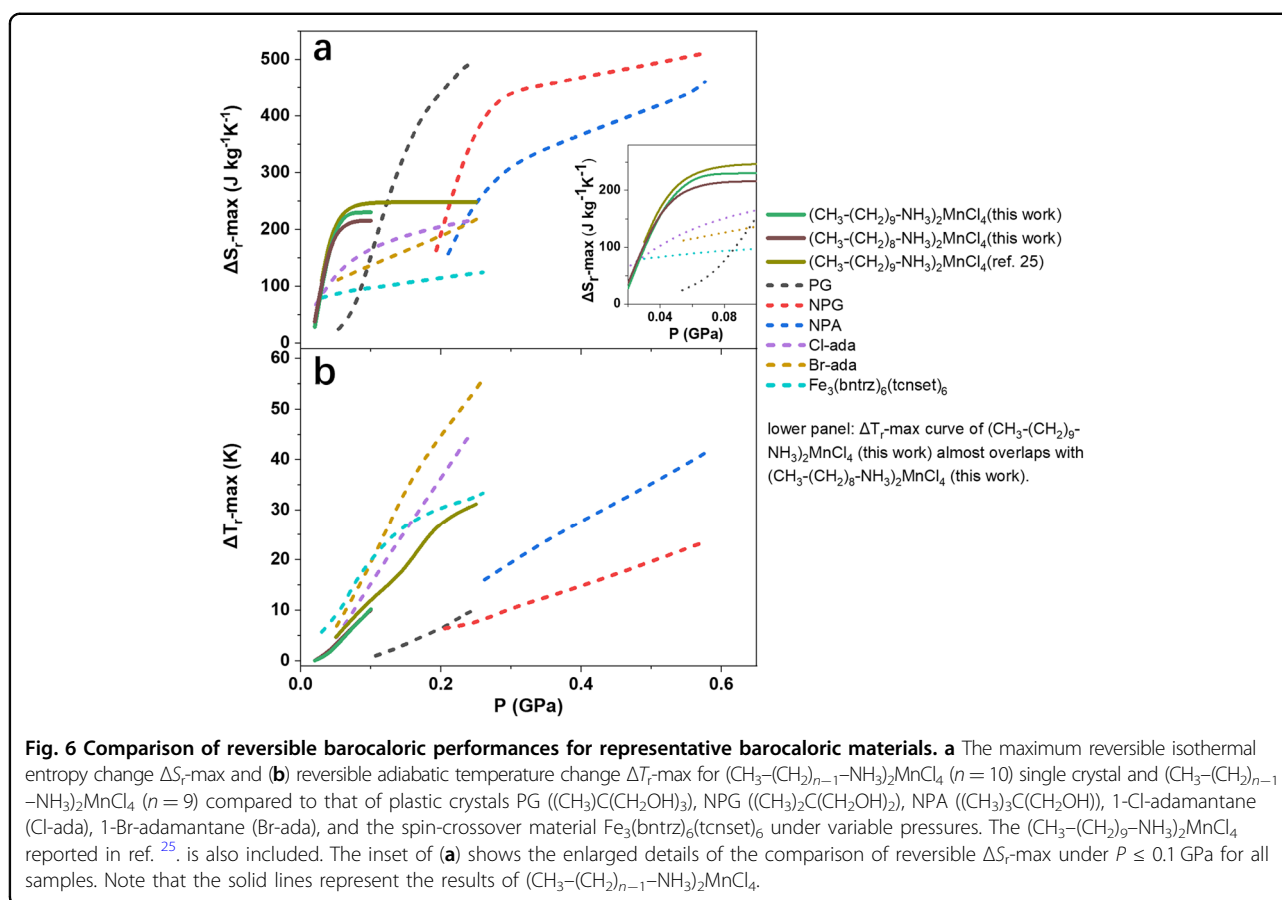
$\Delta S_p \sim 212$ J kg^{-1} K^{-1} (Fig. S19). Under 0.1 GPa, ΔT_p reaches ~15 K and ~14 K for $n = 10$ and $n = 9$, respectively (Fig. 5d and Fig. S20). Moreover, the reversible ΔS_r (Fig. 5e and Fig. S21) is reckoned as the overlap of the ΔS_p of compression and decompression, while similarly, the reversible ΔT_r (Fig. 5f and Fig. S22) is obtained, excluding the influence of thermal hysteresis[10,19]. At 0.08 GPa, the reversible entropy change reaches its maximum. $\Delta S_r \sim 230$ and ~ 212 J kg^{-1} K^{-1} for $n = 10$ and $n = 9$, respectively (Fig. 5e and Fig. S21), while the reversible ΔT_r is the same at 0.1 GPa ($\Delta T_r \sim$ 10 K for both) (Fig. 5f and Fig. S22). which can be understandable noting that the $n = 9$ (~172 K GPa^{-1}) shows higher pressure sensitivity than $n = 10$ (~150 K GPa^{-1}), see Table 2.

Furthermore, we compare the reversible barocaloric capacities of (CH$_3$–(CH$_2$)$_{n-1}$–NH$_3$)$_2$MnCl$_4$ ($n = 9,10$) with those of other representative reported barocaloric materials, including the plastic crystals PG ((CH$_3$)C(CH$_2$OH)$_3$)[13,17], NPG ((CH$_3$)$_2$C(CH$_2$OH)$_2$)[13,17], NPA ((CH$_3$)$_3$C(CH$_2$OH))[13,17], 1-Cl-adamantane (Cl-ada)[19], 1-Br-adamantane (Br-ada)[19],

and the material with spin-crossover Fe$_3$(bntrz)$_6$(tcnset)$_6$[20]. As shown in Fig. 6 and the inset, at low pressures (less than 0.1 GPa), the achievable maximum ΔS_r of (CH$_3$–(CH$_2$)$_{n-1}$–NH$_3$)$_2$MnCl$_4$ ($n = 9,10$) is remarkably higher than that of other reported materials, while the ΔT_r is also competitive, which indicates the attractive forces of the (CH$_3$–(CH$_2$)$_{n-1}$–NH$_3$)$_2$MnCl$_4$ ($n = 9,10$) among refrigerants applied under low-pressure conditions.

Conclusions

In conclusion, for the emergent colossal reversible BCE in organic-inorganic perovskite hybrids (CH$_3$–(CH$_2$)$_{n-1}$–NH$_3$)$_2$MnCl$_4$ ($n = 9,10$), we successfully grew a single crystal, and the underlying mechanism was determined by high-resolution SC-XRD, IR spectroscopy and DFT calculations. The (CH$_3$–(CH$_2$)$_{n-1}$–NH$_3$)$_2$MnCl$_4$ ($n = 10$) single crystal undergoes a structural transformation from a monoclinic layered perovskite into a tetragonal structure around $T_s \sim 311.5$ K. However, the rigid conformation of the (CH$_3$–(CH$_2$)$_9$–NH$_3$)$^+$ organic chains attaching to MnCl$_4^{2-}$ inorganic frameworks becomes unobservable,

Fig. 6 Comparison of reversible barocaloric performances for representative barocaloric materials. a The maximum reversible isothermal entropy change ΔS_r-max and (**b**) reversible adiabatic temperature change ΔT_r-max for $(CH_3–(CH_2)_{n-1}–NH_3)_2MnCl_4$ ($n = 10$) single crystal and $(CH_3–(CH_2)_{n-1}–NH_3)_2MnCl_4$ ($n = 9$) compared to that of plastic crystals PG $((CH_3)C(CH_2OH)_3)$, NPG $((CH_3)_2C(CH_2OH)_2)$, NPA $((CH_3)_3C(CH_2OH))$, 1-Cl-adamantane (Cl-ada), 1-Br-adamantane (Br-ada), and the spin-crossover material $Fe_3(bntrz)_6(tcnset)_6$ under variable pressures. The $(CH_3–(CH_2)_9–NH_3)_2MnCl_4$ reported in ref. [25]. is also included. The inset of (**a**) shows the enlarged details of the comparison of reversible ΔS_r-max under $P \leq 0.1$ GPa for all samples. Note that the solid lines represent the results of $(CH_3–(CH_2)_{n-1}–NH_3)_2MnCl_4$.

and only $MnCl_6$ octahedra can be detected, but its obvious distortion due to tight bonding of organic moieties disappears at high temperatures. All these points to the highly disordered organic chains above the T_s. The IF spectra give fingerprint information across T_s for each component, i.e. the NH_3 head, the CH_2 and $C–C$ chains, and the CH_3 tails, in the entire $(CH_3–(CH_2)_9–NH_3)^+$ chains, which disclose the nature of drastic transformation from ordered rigidity to disordered flexibility and explains the huge phase-transition entropy comparable to melting entropy of organic chains. Moreover, the DFT calculations combined with the experimental observations give the possible conformation of the organic chains above the T_s. The large entropy change and the small hysteresis as low as 2.6 K ($0.1\,K\,min^{-1}$) and 4.0 K ($1\,K\,min^{-1}$) related closely to the specific hybrid organic–inorganic structure and single-crystal nature leads to the colossal reversible BCE. The excellent barocaloric performance of $(CH_3–(CH_2)_{n-1}–NH_3)_2MnCl_4$ emphasizes the sufficient significance of the entropy derived from the conformational disorder of organic chains. One can explore many more organic–inorganic hybrid materials with analogous barocaloric mechanisms, which are promising for facilitating barocaloric refrigeration.

Author details
[1]Beijing National Laboratory for Condensed Matter physics, Institute of Physics, Chinese Academy of Sciences, 100190 Beijing, P. R. China. [2]School of Physical Sciences, University of Chinese Academy of Sciences, 101408 Beijing, China. [3]Songshan Lake Materials Laboratory, 523808 Dongguan, Guangdong, P. R. China. [4]Fujian Innovation Academy, Chinese Academy of Sciences, 350108 Fuzhou, Fujian, China. [5]Ganjiang Innovation Academy, Chinese Academy of Sciences, 341000 Ganzhou, Jiangxi, China. [6]NIST Center for Neutron Research, National Institute of Standards and Technology, Gaithersburg, MD 20899, USA. [7]Ningbo Institute of Materials Technology & Engineering, Chinese Academy of Sciences, 315201 Ningbo, Zhejiang, China

Author contributions
F.H. B.S., and J.H. conceived the project idea. F.H. Y.G. J.H. J.W. Q.H., and B.S. designed the experiments. Y.G. and X.L. grew the single crystals. H.Z. Y.W. and B.W. helped to prepare the samples. H.L. and Y.G. collected the SC-XRD data. Y.G. Y-T.S. H.L., and Y-G.S. analyzed the SC-XRD data. F.S. Q.H. C.Z., and Z.Y. helped with the structural analysis. Y.G. and H.Z. performed the IR spectroscopy

measurements and analysis, and Y-L.L. further confirmed and analyzed the spectra. Y.G. and H.S. performed the DFT calculations and analysis. Y.G. measured and analyzed the barocaloric performance. Z-B.Y. helped with the barocaloric measurements. Z.T, Y.L. Y.C. Y-G.S. T.Z., and J.S. participated in fruitful discussions. Y.G. and F.H. wrote and edited the manuscript with discussion and input from all coauthors.

Conflict of interest
The authors declare no competing interests.

References
1. Moya, X., Kar-Narayan, S. & Mathur, N. D. Caloric materials near ferroic phase transitions. *Nat. Mater.* **13**, 439–450 (2014).
2. Yuce, S. et al. Barocaloric effect in the magnetocaloric prototype $Gd_5Si_2Ge_2$. *Appl. Phys. Lett.* **101**, 071906 (2012).
3. Matsunami, D., Fujita, A., Takenaka, K. & Kano, M. Giant barocaloric effect enhanced by the frustration of the antiferromagnetic phase in Mn_3GaN. *Nat. Mater.* **14**, 73–78 (2015).
4. Stern-Taulats, E. et al. Reversible adiabatic temperature changes at the magnetocaloric and barocaloric effects in $Fe_{49}Rh_{51}$. *Appl. Phys. Lett.* **107**, 152409 (2015).
5. Mañosa, L. et al. Inverse barocaloric effect in the giant magnetocaloric La-Fe-Si-Co compound. *Nat. Commun.* **2**, 595 (2011).
6. Mikhaleva, E. A. et al. Caloric characteristics of $PbTiO_3$ in the temperature range of the ferroelectric phase transition. *Phys. Solid State* **54**, 1832–1840 (2012).
7. Stern-Taulats, E. et al. Inverse barocaloric effects in ferroelectric $BaTiO_3$ ceramics. *APL Mater.* **4**, 091102 (2016).
8. Lloveras, P. et al. Giant barocaloric effects at low pressure in ferrielectric ammonium sulphate. *Nat. Commun.* **6**, 8801 (2015).
9. Aznar, A. et al. Giant and reversible inverse barocaloric effects near room temperature in ferromagnetic $MnCoGeB_{0.03}$. *Adv. Mater.* **31**, 1903577 (2019).
10. Aznar, A. et al. Giant barocaloric effects over a wide temperature range in superionic conductor AgI. *Nat. Commun.* **8**, 1851 (2017).
11. Bermudez-Garcia, J. M. et al. Giant barocaloric effect in the ferroic organic-inorganic hybrid [TPrA][Mn(dca)$_3$] perovskite under easily accessible pressures. *Nat. Commun.* **8**, 15715 (2017).
12. Li, B. et al. Colossal barocaloric effects in plastic crystals. *Nature* **567**, 506–510 (2019).
13. Lloveras, P. et al. Colossal barocaloric effects near room temperature in plastic crystals of neopentylglycol. *Nat. Commun.* **10**, 1803 (2019).
14. Cazorla, C. & Errandonea, D. Giant mechanocaloric effects in fluorite-structured superionic materials. *Nano Lett.* **16**, 3124–3129 (2016).
15. Imamura, W. et al. Supergiant barocaloric effects in acetoxy silicone rubber over a wide temperature range: great potential for solid-state cooling. *Chin. J. Polym. Sci.* **38**, 999–1005 (2020).
16. Li, F. B. et al. Understanding colossal barocaloric effects in plastic crystals. *Nat. Commun.* **11**, 4190 (2020).
17. Aznar, A. et al. Reversible and irreversible colossal barocaloric in plastic cystals. *J. Mater. Chem. A* **8**, 639 (2020).
18. Yoshida, Y., Yuse, K, Guyomar, D., Capsal, J.-F. & Sebald, G. Elastocaloric effect in poly(vinylidene fluoride-trifluoroethylene-chlorotrifluoroethylene) terpolymer. *Appl. Phys. Lett.* **108**, 242904 (2016).
19. Aznar, A. et al. Reversible colossal barocaloric effects near room temperature in 1-X-adamantane (X=Cl, Br) plastic crystals. *Appl. Mater. Today* **23**, 101023 (2021).
20. Romanini, M. et al. Giant and reversible barocaloric effect in trinuclear spin-crossover complex Fe$_3$ (bntrz)$_6$ (tcnset)$_6$. *Adv. Mater.* **33**, 2008076 (2021).
21. Silva, D. J., Ventura, J. & Araújo, J. P. Caloric devices: a review on numerical modeling and optimization strategies. *Int. J. Energy Res.* 1–42, https://doi.org/10.1002/er.7023 (2021).
22. Aprea, C., Greco, A., Maiorino, A. & Masselli, C. The use of barocaloric effect for energy saving in a domestic refrigerator with ethylene-glycol based nano-fluids: a numerical analysis and a comparison with a vapor compression cooler. *Energy* **190**, 116404 (2020).
23. Mitzi, D. B. Synthesis, structure, and properties of organic-inorganic perovskites and related materials. *Prog. Inorg. Chem.* **48**, https://doi.org/10.1002/9780470166499.ch1 (1999).
24. Li, W. et al. Study of solid-solid phase change of (n-C$_n$H$_{2n+1}$NH$_3$)$_2$MCl$_4$ for thermal energy storage. *Thermochim. Acta* **326**, 183–186 (1999).
25. Li, J. et al. Colossal reversible barocaloric effects in layered hybrid perovskite (C$_{10}$H$_{21}$NH$_3$)$_2$ MnCl$_4$ under low pressure near room temperature. *Adv. Funct. Mater.* **31**, 2105154 (2021).
26. Mitzi, D. B. Synthesis structure, and properties of organic-inorganic perovskites and related materials. *Prog. Inorg. Chem* **48**, 1–121 (1999).
27. Liu, Y., Di, Y., He, D., Zhou, Q. & Dou, J. Crystal structures, lattice potential energies, and thermochemical properties of crystalline compounds (1-C$_n$H$_{2n+1}$NH$_3$)$_2$ZnCl$_4$(s)(n=8, 10,12, and 13). *Inorg. Chem.* **50**, 10755–10764 (2011).
28. Casal, H. L., Cameron, D. G. & Mantsch, H. H. A vibrational spectroscopic characterization of the solid-phase behavior of n-decylammonium chloride (n-C10H21NH3Cl) and bis(n-decylammonium) tetrachlorocadmate [(n-C10H21NH3)2CdCl4]. *J. Phys. Chem.* **89**, 5557–5565 (1985).
29. Barman, S., Venkataraman, N. V., Vasudevan, S. & Seshadri, R. Phase transitions in the anchored organic bilayers of long-chain alkylammonium lead iodides (C$_n$H$_{2n+1}$NH$_3$)$_2$PbI$_4$, n = 12, 16, 18. *J. Phys. Chem. B* **107**, 1875–1883 (2003).
30. Jalbout, A. F., Ouasri, A., Jeghnou, H. & Rhandour, A. Experimental and theoretical studies of monoalkylammonium hexafluorosilicate [CH3(CH2)nNH3]2SiF6 (n = 2, 3) and ethylammonium hexafluorosilicate [(C2H5)2NH2]2SiF6. *Vib. Spectrosc.* **44**, 94–100 (2007).
31. MacPhail, R. A., Straws, H. L. & Snyder, R. G. C.-H. stretching modes snyder, R. G. C-H stretching modes and the structure of n-alkyl chains. 2. long, all-trans chains. *J. Phys. Chem.* **88**, 334–341 (1984).
32. Guillaume, F. et al. Molecular motions of decylammonium chains in the perovskite type layered compound (C$_{10}$H$_{21}$NH$_3$)$_2$MnCl$_4$. *Mol. Phys.* **67:3**, 665–679 (1989).
33. Manosa, L. & Planes, A. Materials with giant mechanocaloric effects: cooling by strength. *Adv. Mater.* **29**, 1603607 (2017).